

Kinetic and Thermodynamic Assessments of the Mediator–Template Assembly of Nanoparticles

I-Im Stephanie Lim, Mathew M. Maye, Jin Luo, and Chuan-Jian Zhong*

Department of Chemistry, State University of New York at Binghamton, Binghamton, New York 13902

Received: September 21, 2004; In Final Form: November 19, 2004

The understanding of kinetic and thermodynamic factors governing the assembly of nanoparticles is important for the design and control of functional nanostructures. This paper describes a study of the kinetic and thermodynamic factors governing the mediator–template assembly of gold nanoparticles into spherical assemblies in solutions. The study is based on spectrophotometric measurements of the surface plasmon (SP) resonance optical property. Gold nanoparticle cores (~ 5 nm) encapsulated with tetraoctylammonium bromide shells were studied as a model system. The mediator–template assembly involves a thioether-based multidentate ligand (e.g., $\text{MeSi}(\text{CH}_2\text{SMe})_3$) which functions as a mediator, whereas the tetraoctylammonium bromide capping molecules function as template agents. On the basis of the temperature dependence of the SP optical property in the mediator–template assembly process, the kinetic and thermodynamic parameters such as the reaction rate constant and reaction enthalpy have been determined. The results led to two important findings. First, the mediator–template assembly of nanoparticles is an enthalpy-driven process. Second, the enthalpy change (-1.3 kcal/mol) is close to the magnitude of the van der Waals interaction energy for alkyl chains and the condensation energy of hydrocarbons. Implications of the findings to the understanding of the interparticle interactions have also been discussed.

Introduction

To exploit the materials properties of nanoparticles, the ability to assemble nanoparticles with controllable sizes, shapes, and interparticle spatial properties is essential. The synthesis of monolayer-protected metal or semiconductor nanoparticles in the size range 1–10 nm^{1–11} has attracted enormous interest for the development of viable strategies in nanoparticle assemblies. Among many strategies, the strategy of encapsulating nanocrystal cores with organic monolayer shells has two major advantages: First, it acts as a protective shell, resisting the propensity of aggregation. Second, the shell molecules can be tailored to define the interfacial chemistry in controllable ways. Many examples that exploit such nanostructured interfacial chemistry have emerged, including ligand-exchange reaction,⁴ layer-by-layer stepwise assembly,⁵ DNA-linked assembly,^{12,13} polymer- or dendrimer-mediated molecular recognition,^{14,15} molecularly mediated exchange cross-linking,^{6–11} and multidentate thioether-mediated assembly.^{16,17} Potential applications of the nanoparticle-structured assemblies include chemical sensing,^{7,18–20} catalysis,^{21–24} drug delivery, nanoelectronics,^{5a,25} and medical diagnostics.^{12,13,26}

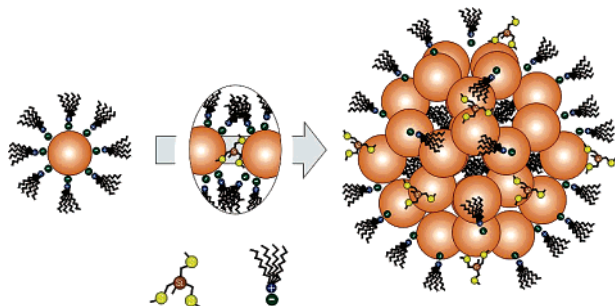
We have recently demonstrated a mediator–template strategy for the assembly of gold nanoparticles into spherical assemblies.^{16,17} In comparison with other assembly techniques, our previous work on an exchange cross-linking route for the assembly of nanoparticles capped with thiolate monolayers on different substrates^{6–11} can be viewed as an initial demonstration of the mediator–template assembly strategy. For example, the hydrogen-bonding-mediated assembly of gold nanoparticles capped with carboxylic-acid-functionalized thiolates involves hydrogen-bonding-mediated interparticle linking and alkyl chain

templated intershell interaction.⁸ For the mediator–template strategy demonstrated for the assembly of gold nanoparticles, one example involved using thioethers (e.g., tetra[(methylthio)methyl]silane ($\text{Si}(\text{CH}_2\text{SCH}_3)_4$, TE_4) and methyltris[(methylthio)methyl]silane ($\text{MeSi}(\text{CH}_2\text{SCH}_3)_3$, TE_3)) and surfactants (e.g., tetraoctylammonium, $[\text{CH}_3(\text{CH}_2)_7]_4\text{N}^+\text{Br}^-$, TOA^+Br^-) as model systems of mediator and template, respectively.^{16,17} This example is illustrated in Scheme 1.

We have shown that the mediator–template assembly of gold nanoparticles leads to size-controllable spherical assemblies in the diameter range 30–200 nm.^{16,17} The spherical shapes were evidenced by both transmission electron microscopy (TEM) and atomic force microscopy (AFM) imaging studies of the assemblies on different substrates. Because of the unprecedented ability of our mediator–template strategy for size and shape control, the understanding of the kinetic and thermodynamic factors governing the assembly of nanoparticles is important for rational design and better control of the functional nanostructures. The work reported herein is aimed at assessing both kinetic and thermodynamic factors in the mediator–template assembly process through measurements of the surface plasmon (SP) resonance optical properties of gold nanoparticles. The spectrophotometric measurements of the SP optical properties for the nanoparticle assembly process were performed at different temperatures. The experimental data allowed us to derive both kinetic and thermodynamic parameters such as the reaction rate constant and reaction enthalpy. Such parameters can be used to gain insight into the understanding of the thermodynamic driving force and the interparticle interactions involved in the mediator–template assembly process. We note that thermodynamic and kinetic characterizations have recently been shown to provide useful information for understanding interactions on surfaces of CdSe nanoparticles when the particles react with ligands in solutions.²⁷

* To whom correspondence should be addressed. E-mail: cjzhong@binghamton.edu.

SCHEME 1. Schematic Illustration of the Mediator–Template Assembly of Gold Nanoparticles Using TE₃ as Mediator and TOA⁺Br[−] as Template.



Experimental Section

Chemicals. Hydrogen tetrachloroaurate (HAuCl₄, 99%), tetraoctylammonium bromide (TOA⁺Br[−], 99%), and sodium borohydride (NaBH₄, 99%) were purchased from Aldrich and used as received. Other chemicals included toluene (99.8%), hexane (99.9%), and ethanol (EtOH, 99.9%). Water was purified with a Millipore Milli-Q water system. The synthesis of methyltris[(methylthio)methyl]silane (MeSi(CH₂SCH₃)₃, TE₃) has been described previously.²⁸

Synthesis. Gold nanoparticles capped with monolayer shells of tetraoctylammonium bromide were synthesized using the two-phase protocol.^{2b} Briefly, TOA⁺Br[−] (0.55 g) was used as a phase-transfer reagent and was added to 32 mL of toluene (~31 mM). After stirring for ~15 min, an aqueous solution (20 mL) of HAuCl₄ (0.077 g) was added under stirring. The AuCl₄[−] ions were completely transferred from the aqueous solution to toluene within 15 min. The color of the final toluene phase turned from colorless to orange-red. After stirring for ~30 min, the organic phase was separated, and the aqueous phase was discarded. With the remaining toluene solution, a tenfold excess of aqueous reducing agent, NaBH₄, was added dropwise into the solution under stirring. The solution turned from orange-red to a deep red color. The reaction was then allowed to continue under stirring at room temperature for 24 h. The aqueous phase of the resulting solution was removed and further treated with drying agent to remove trace water. The resulting toluene solution contained gold nanoparticles (Au_{nm}) capped with TOA⁺Br[−], which are abbreviated as TOA-capped Au_{nm}. The particles have an average diameter of 4.6 ± 0.8 nm.

Instrumentation. UV–visible (UV–vis) spectrophotometric spectra were acquired with an HP 8453 spectrophotometer. The spectra were collected over the range 200–1100 nm. TEM was performed on a Hitachi H-7000 electron microscope (100 kV). The gold nanoparticle samples were dissolved in toluene solution and drop-cast onto a carbon-coated copper grid sample holder, followed by evaporation in air at room temperature.

Experimental Procedures. The assembling reactions between TE₃ and TOA-capped Au_{nm} were carried out under controlled temperatures and monitored using a UV–visible spectrophotometer. The cuvette had a path length of 1 cm. Initial Au_{nm} concentrations were determined via Beer's law and estimated using the average diameters of the particles. The molar absorptivity (ε_{Au}) for the 4.6 ± 0.8 nm gold nanoparticles was measured to be 8.8 × 10⁶ M^{−1}·cm^{−1}.²⁹ Diluted solutions of gold nanoparticles (0.1 μM, 1.5 mL) in toluene were utilized. A stock solution of 10 mM TE₃ was quantitatively added (3 μL) into the nanoparticle solution using a micropipet. The solution was quickly mixed by purging for ~2 s before the measurement. We found that this purging time was sufficient to mix the small volume (1.5 mL) solution effectively.

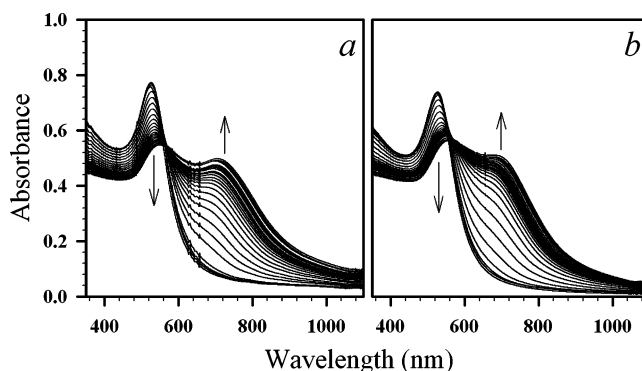


Figure 1. UV–vis spectral evolution for the assembly of Au_{nm} upon addition of TE₃ ([TE₃] = 20 μM, [Au_{nm}] = 0.1 μM). The reaction temperatures are 5 °C (a) and 22 °C (b). The spectral evolutions were recorded within the time frame of 1 h, and the arrows shown in the graphs indicate the directions of the spectral evolution vs time (The actual time interval for each curve can be found in Figure 4.)

To control the desired temperature for each measurement, a quartz cuvette with a built-in liquid flow cell connected to a temperature controller was used. The liquid flow was controlled by a mechanical pump. For temperatures below room temperature, nitrogen gas was used to prevent water condensation on the optical window. To obtain temperatures below 0 °C, a combination of dry ice and ethanol solvent was used. For the measurements around 0 °C, crushed ice was utilized. To maintain the temperature around 15 °C, we used *p*-xylene and liquid N₂. For temperatures above 25 °C, a heating controller (Glas-Col, Digi Trol II) was utilized to control the temperature. Actual temperatures in the reaction solution were measured by immersing a thermocouple into the cuvette during the reaction.

Results and Discussion

Spectrophotometric Measurements. Gold nanoparticles of ~5-nm-diameter core size exhibit a strong SP band in the visible region (525 nm), which can be monitored by UV–vis spectrophotometric measurements during the process of nanoparticle assembly.^{9,16,17,26} The wavelength and absorbance of the band depend on particle size, shape, and interparticle dielectric medium properties. On the basis of Mie theory,³⁰ the surrounding medium dielectric constants, particle size, and interparticle distance all play important roles in the SP resonance. Recent work has shown that the SP band of gold nanoparticles changes upon assembly,^{16,17} and the size of the assembly depends on the TE₃–Au_{nm} molar ratio in the range 1–2000.¹⁷ To understand the kinetic and thermodynamic factors governing the assembly process, we have closely monitored the spectral evolution of the SP band.

Figure 1 shows a typical set of UV–vis spectra for a toluene solution with a TE₃–Au_{nm} molar ratio of ~200. The spectral evolution shown here was collected at two different temperatures below room temperature. The general trend observed from Figure 1 is the gradual decrease of the SP band at ~525 nm and the increase of a new band at a longer wavelength (~700 nm). The spectral evolution was also accompanied by a distinct color change from red to bluish purple. The spectral shift to the higher wavelength and the accompanying color change are indicative of a change in interparticle distance or dielectric medium properties as a result of the nanoparticle assembly.^{16,17} Below room temperature, the spectral evolution clearly displays an isosbestic point at ~560 nm. The observation of such an isosbestic point implies the presence of two distinct light-absorbing species in the solution.^{16,17,27}

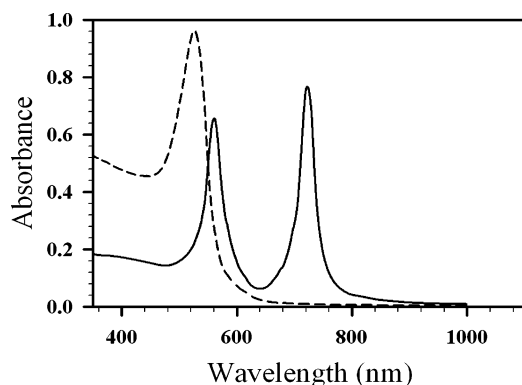


Figure 2. Simulated UV-vis spectra for individual Au nanoparticles of 5-nm core size (dashed line) and spherical assemblies of the nanoparticles (solid line).

The two chemical species associated with the two SP bands are ascribed to individual Au nanoparticles and spherical assemblies of the nanoparticles. Figure 2 shows a set of theoretically simulated spectra of the experimental data in Figure 1 based on Mie theory.³⁰ Details for our simulation have been recently reported.³¹ Two important parameters for the simulations involved the volume concentration of nanoparticles and dielectric medium constant (ϵ). In comparison with $\epsilon = 1.9$ obtained for the spectrum of the individual Au nanoparticles, we obtained $\epsilon = 3.5$ and 9.4 for the 525-nm and 710-nm bands, respectively, in the spectrum for the spherical assemblies of nanoparticles. In these simulations, we also found that the volume concentration of nanoparticles was reduced from individual nanoparticles to spherical assemblies. These changes are indicative of changes in interparticle distances and dielectric medium properties. Similar simulation results have also been obtained using modified Mie theory,³² the details of which will be described in a separate report. To quantitatively assess the individual species with the experimental data in Figure 2, we performed both spectral deconvolution and peak integration. In view of the presence of the well-defined isosbestic point and earlier work of using integrated peak area for assessing nanoparticle aggregation,³³ we consider that the integrated area (e.g., from 560 nm (isosbestic point) to 1100 nm) can more appropriately represent the change in optical property (i.e., the cross-section of the band). The integration was performed by setting a vertical line at the isosbestic point as the border of the two SP bands, which were found to approximate the spectral deconvolution reasonably well. We further note that because of the presence of the isosbestic point the spectral evolution at the early stage of the assembly is not simply a red shift of the SP band corresponding to the Au nanoparticles; it is due to the SP band corresponding to the spherical assemblies.

Figure 3 shows another set of UV-vis spectra which were collected above room temperature. In comparison with the spectral evolution below room temperature (Figure 1), the data above room temperature (Figure 3) showed significant differences in band features. Although there is an indication of a decrease for the SP band at ~525 nm and increase for a new band at a longer wavelength (~575 nm), these two spectral features are significantly overlapped. The spectral broadening to longer wavelength for the long-wavelength SP band is evident. In comparison with the lower-temperature data, the initial change of the long-wavelength band at the higher temperatures (Figure 3) is relatively fast.

In these experiments, a dramatic color change from red to bluish purple immediately following the addition of TE₃ to the Au_{nm} solution was evident, which was consistent with the rapid

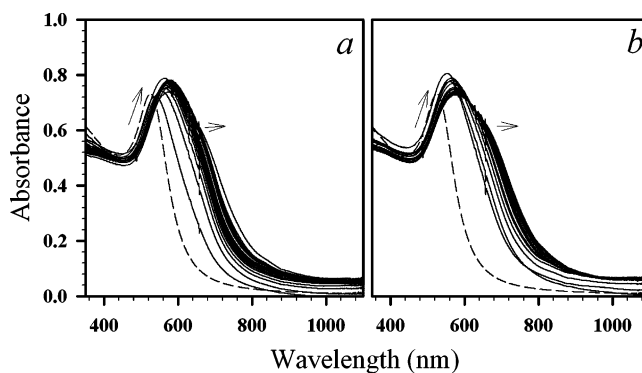
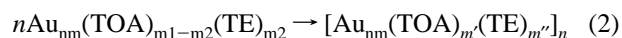
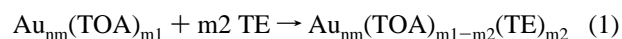


Figure 3. UV-vis spectral evolution for the assembly of Au_{nm} upon addition of TE₃ ([TE₃] = 20 μ M, [Au_{nm}] = 0.1 μ M). The reaction temperatures are 45 °C (a) and 90 °C (b). The spectral evolutions were recorded within the time frame of 1 h, and the arrows shown in the graphs indicate the directions of the spectral evolution vs time (The actual time interval for each curve is similar to those found in Figure 5.)

initial spectral evolution. In general, the colors of the solutions for those from above room temperature appeared to be much darker than those below room temperature. The time needed for the precipitation of the reaction product from the solutions at the lower temperatures (~3 h) was much shorter than those at higher temperatures (~3 days). Our experiment showed differences in reaction rates at different temperatures. By examining the morphology of the reaction products using TEM in a separate experiment, we found that the nanoparticle assemblies display a spherical morphology with monodispersed sizes, in agreement with those reported in our previous work.¹⁷ While the rate for the formation of spherical assemblies is a function of temperature, relatively insignificant differences were found from different samples for the average sizes of the spherical assemblies obtained at different temperatures. We also note that spherical sizes are found to be dependent on the concentration ratio, the particle size, mediator structure, and the template structure. A detailed assessment of these parameters is part of our ongoing work. The work reported in this paper focuses mainly on the relationship between nanoparticle assemblies and reaction time for the assessment of the kinetic and thermodynamic factors governing the nanoparticle assembly process.

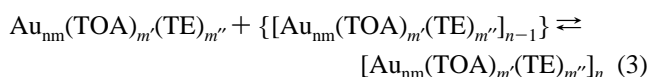
Kinetic and Thermodynamic Assessments of Optical Properties. Although both absorption and scattering phenomena are involved in the optical property of nanoparticles, the absorptivity is believed to be much more significant than light scattering in view of the large molar absorptivity ($\sim 10^7$ – 10^8 M⁻¹ cm⁻¹) for the gold nanoparticles under our investigation. As such, the measurement of absorptivity provides an effective means to monitor the concentration changes of nanoparticles and spherical assemblies. The spectral evolution is further analyzed in terms of the time dependence in absorbance or integrated peak area of the SP band. To derive the kinetic relationships, we first consider the following two types of reactions involved in the TE₃-mediated assembly of TOA-capped gold nanoparticles:



where $m1$ and $m2$ stand for the number of ligands in the initial exchange reaction (eq 1), whereas m' and m'' stand for the total numbers of TOA and TE₃ ligands in the final assembly product

as a result of the interparticle cross-linking reaction (eq 2). n represents the average number of nanoparticles in the spherical assembly.

If we assume that the initial exchange reaction (eq 1) is relatively fast and the subsequent reactions involve interparticle cross-linking, the nucleation and growth of the nanoparticle assembly (eq 2) is relatively slow. We can then consider eq 2 as an apparent rate-determining step. The assumption is not unrealistic in view of the relatively strong chemical affinity of thioether ligands to gold and the shell structural effect in directing aggregation or growth of the nanoparticles and assemblies. The fact that a higher mediator-to-template ratio leads to smaller-sized nanoparticle assembly than that for a lower ratio^{16,17} supports the assumption of facile ligand-exchange reaction in the mediator–template assembly. The exchanged ligand has in fact been detected by X-ray photoelectron spectroscopy (XPS) analysis of the nanoparticle assemblies (not shown). We further assume that, once a nucleus is formed, the reaction rate for each individual step in the apparent rate-determining reaction is proportional to the concentration of the incoming Au nanoparticles (first-order reaction). This assumption is also not unreasonable in view of the much larger surface area of the growing spherical assembly than that of a single nanoparticle. We can basically describe the growing spherical assembly as a large solid surface. With these assumptions, we consider the following scheme for the growth of the nanoparticle assembly



For simplicity, we use C_{Au} to represent $[\text{Au}_{\text{nm}}(\text{TOA})_m(\text{TE})_{m''}]$ (concentration of Au nanoparticles at time t), $C_{(\text{Au})_n}$ to represent $[[\text{Au}_{\text{nm}}(\text{TOA})_m(\text{TE})_{m''}]_n]$ (concentration of nanoparticle assembly at time t), and $\{[\text{Au}_{\text{nm}}(\text{TOA})_m(\text{TE})_{m''}]_{n-1}\}$ to indicate its reacting surface nature of the growing assembly. Using k_+ and k_- to further denote the forward and backward reaction rate constants, respectively, we can express the rate equation (first-order) for the nanoparticle assembly as

$$\frac{dC_{(\text{Au})_n}}{dt} = k_+ C_{\text{Au}} - k_- C_{(\text{Au})_n} \quad (4)$$

By integrating eq 4 and considering $C_{\text{Au}}(0) (=C^0) = C_{\text{Au}} + nC_{(\text{Au})_n}$, where $C_{\text{Au}}(0)$ represents the initial concentration of the Au nanoparticles, we can derive the rate equations for both the spherical assemblies and the Au nanoparticles

$$C_{(\text{Au})_n} = C'(1 - e^{-kt}) \quad (5)$$

$$C_{\text{Au}} = C'(C'' + e^{-kt}) \quad (6)$$

where $C' = k_+ C^0 / (nk_+ + k_-)$, $C'' = [(n-1)k_+ + k_-] / k_+$, and k (apparent rate constant) $= nk_+ + k_-$. By relating concentration to absorbance according to Beer's law, we can rewrite eqs 5–6 as

$$\text{Abs}_{(\text{Au})_n} = A_1'(1 - e^{-kt}) \quad (7)$$

$$\text{Abs}_{\text{Au}} = A_2' + A_2''e^{-kt} \quad (8)$$

where $A_1' = C'\epsilon_{(\text{Au})_n}$, $A_2' = C'C''\epsilon_{\text{Au}}$, and $A_2'' = C'\epsilon_{\text{Au}}$. $\epsilon_{(\text{Au})_n}$ and ϵ_{Au} are extinction coefficients of Au nanoparticles and spherical assemblies, respectively.

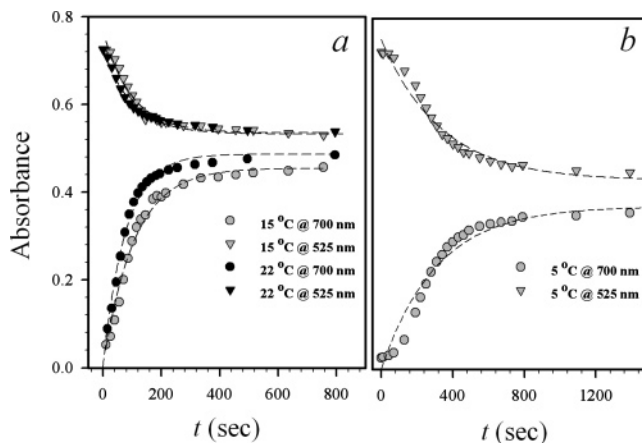


Figure 4. Plots of absorbance vs time for the SP bands at 520 nm (▽) and 700 nm (○) for the reactions at 15 and 22 °C (a) and 5 °C (b).

TABLE 1: Summary of the Fitting Results from the Processed UV–vis Data (Figures 4 and 5) Using Eqs 7–8

<i>T</i> (°C)	<i>k</i> (s ^{−1})		<i>k</i> (s ^{−1})	
	absorbance		area	
	525 nm	700 nm	440–560 nm	560–1100 nm
−2	0.0015	0.0023	0.0029	0.0032
5	0.0027	0.0038	0.0033	0.0039
15	0.0074	0.0078	0.0072	0.0088
22	0.0112	0.0130	0.0133	0.0140
30	0.0164	0.0166	0.0142	0.0154
45	0.0182	0.0175	0.0167	0.0164

We note the fact that the absorbance at 525 nm in the UV–vis spectra (see Figures 1 and 3) decreases to a constant minimum even after the apparent completion of the reaction. While the origin of this phenomenon is not completely clear at this time and is under further investigation, we examined the fitting of eqs 7–8 to the experimental data. Figure 4 shows a typical set of absorbance vs time plots obtained below room temperature. In general, the absorbance at 700 nm (○) shows an exponential rise to a plateau, whereas the absorbance at 525 nm (▽) displays a gradual decrease to a constant value. Similar trends were observed for reactions at other temperatures (not shown). A major difference between the data above and below room temperature is the time length required for the absorbance to reach a constant value. The data above room temperature showed a fast reaction rate. The dashed lines in Figure 4 are fitting results based on eqs 7–8. At these low temperatures, the absorbance vs time data can be fitted very well. The fitting results exhibited an increase in the apparent rate constant (k) as a function of temperature (Table 1). At higher temperatures, the fitting was less satisfactory, partly due to overlapping of the SP bands, which makes it difficult to precisely determine the absorbance values.

In view of the band-broadening effect in the longer wavelength region for the 700-nm SP band, we also processed and analyzed the data in terms of the integrated peak area.³³ Because the absorbance (Abs) \propto area, we used the integrated area values to substitute for Abs in eqs 7–8, which were then used for fitting the experimental data. The results are shown in Figure 5 for a typical set of peak area vs time plots. The peak area was integrated from 560 nm (isosbestic point) to 1100 nm in the corresponding UV–vis spectra. The data exhibit a trend very similar to the Abs vs time plots in Figure 4. It is evident that the area–time data were fitted very well by eqs 7–8. The fitting results also showed an increase of the apparent rate constant (k) as the temperature increases.

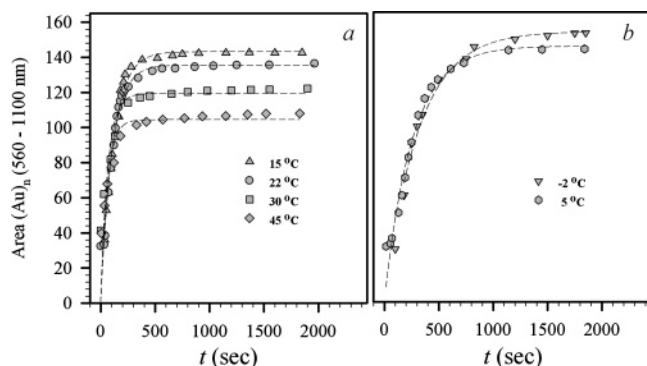


Figure 5. Plots of the peak area (peak areas are integrated from 560 (isosbestic point) to 1100 nm by setting a vertical line at the isosbestic point as the border of the two SP bands) vs time for reactions at several temperatures: 15, 22, 30, and 45 °C (a), and -2 and 5 °C (b).

Table 1 summarizes the kinetic fitting results of the experimental data. We can observe quite consistent results for the rate constants derived from both absorbance and peak area data fittings and from SP bands for both individual nanoparticles and spherical assemblies. The average variation is less than ~10%. Overall, we have observed an increase in the apparent rate constants (k) with increasing temperature, which is consistent with our expectation for the nanoparticle assembly. It is also instructive to compare the magnitude of these apparent rate constants with those derived from other similar nanoparticle assemblies. For example, rate constants of 1.6×10^{-4} and $2.3 \times 10^{-3} \text{ s}^{-1}$ were obtained for 1,9-nonanedithiol- and 11-mercaptoundecanoic acid-mediated thin-film assemblies of gold nanoparticles of a similar size (at room temperature), respectively.¹⁸ In another example, we found that the apparent rate constant of homocysteine- and cysteine-mediated nanoparticle assemblies in aqueous solutions were 0.3 and 0.003 s^{-1} (at room temperature), respectively.²⁶ It is interesting that the apparent rate constant at room temperature for the thioether-mediated assembly in organic solution is ~1–2 orders of magnitude smaller than those for the thin-film assemblies from organic solutions and falls between those for homocysteine- and cysteine-mediated nanoparticle assemblies in aqueous solutions (by a factor of ~3). The former situation can be understood because thin-film assembly requires additional activation energy in the desolvation process. In the latter case, the difference in nucleation and solvation between the different solvents and mediators could lead to a difference in the overall activation energy. A further correlation of these structural and energetic properties should provide important insights into the mechanisms of the molecularly mediated nanoparticle assemblies, which is part of our ongoing work.

On the basis of the experimental data, we further assess the thermodynamic properties of the nanoparticle assembly. Our assessment starts from the consideration of the relationships between the reaction's Gibbs free energy (ΔG), enthalpy (ΔH), entropy (ΔS), and equilibrium constant (K_{eq})

$$\ln K_{\text{eq}} = -\frac{\Delta H}{RT} + \frac{\Delta S}{R} \quad (9)$$

By relating K_{eq} to concentration and absorbance according to Beer's law, we derive

$$\ln \left(\frac{\text{Abs}_{(\text{Au})_n}}{\text{Abs}_{\text{Au}}} \right) = -\left(\frac{\Delta H}{R} \right) \frac{1}{T} + \left(\frac{\Delta S}{R} - \ln \frac{\epsilon_{\text{Au}}}{\epsilon_{(\text{Au})_n}} \right) \quad (10)$$

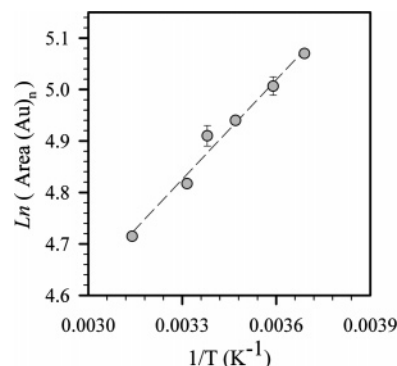


Figure 6. Plots of $\ln(\text{Area}(\text{Au})_n)$ (from peak area data integrated from 560 to 1100 nm) vs $1/T$ (K^{-1}). ($r^2 = 0.981$)

A similar equation can also be written if we use integrated peak area to substitute for absorbance ($\text{Abs} \propto \text{area} \propto \{[\text{Au}_{\text{nm}}(\text{TOA})_{m'}(\text{TE})_{m''}]_n\}$)

$$\ln \left[\frac{\text{Area}_{(\text{Au})_n}}{(\text{Area}_{\text{Au}})^n} \right] = -\left(\frac{\Delta H}{R} \right) \frac{1}{T} + \text{const} \quad (11)$$

We have used both absorbance and peak area data for the thermodynamic analysis. As stated earlier, the integrated peak area (e.g., from 560 nm (isosbestic point) to 1100 nm) can more appropriately represent the change in optical property of all the nanoparticle assemblies (i.e., the cross-section of the band). Furthermore, the concentration of the free gold nanoparticles should be relatively constant upon reaching equilibrium regardless of the temperature. Therefore, the equilibrium values of Abs or area for Au nanoparticles (i.e., $\ln(\text{Area}_{\text{Au}})^n$) at different temperatures are relatively constant. This assumption is largely based on the fact that relatively little change has been observed upon apparent completion of the reaction and under different temperatures (more experiments are needed to confirm the assumption). Equation 11 is thus simplified by rearrangement

$$\ln(\text{Area}_{(\text{Au})_n}) = -\left(\frac{\Delta H}{R} \right) \frac{1}{T} + \text{const} \quad (12)$$

Using the peak integration data obtained by fitting the kinetic data (Figure 5), we can plot $\ln[\text{Area}_{(\text{Au})_n}]$ vs $1/T$, as shown in Figure 6 for a representative set of results. The data display a closely linear relationship, in agreement with eq 12. From the slope (658.6 K), we obtained $\Delta H \approx -5.5 \text{ kJ/mol}$ (or -1.3 kcal/mol). This value is indicative of the exothermic character of the assembly reaction. Although the intercept value at the y-axis could, in principle, provide an estimate of ΔS , the complication of the constant in eq 12 that involves many other factors prevented us from making this estimation at this time. We also note that similar ΔH values have also been obtained from the absorbance data at several different wavelengths under the SP band corresponding to the spherical assembly.

Two major findings can be arrived at on the basis of these analyses. First, the negative sign of ΔH indicates that our mediator–template assembly is an enthalpy-driven process. This is an important finding because the entropy change is expected to be negative for the assembly process (it is a decrease in randomness from dispersed nanoparticles to the formation of the spherical assemblies), given the fact that assembly is a spontaneous process. Second, the determined ΔH , -1.3 kcal/mol , is found to be quite close to the magnitude of van der Waals interaction energy (cohesive energy) for alkyl chains ($\sim 1.4\text{--}1.8 \text{ kcal/mol}$)^{34a} and slightly lower than the

condensation energy of hydrocarbons (~ 6 kcal/mol).^{34b} The determined ΔH value is indicative of the dominance of van der Waals interaction in the mediator–template assembly of the nanoparticles. In comparison, we note that the ΔH value recently determined for the interaction of butylamine on surfaces of CdSe nanoparticles (~ 10 kcal/mol)²⁷ is indicative of the dominance of the surface binding nature.

While the findings are significant, other contributions to the enthalpy change could also be operative. One possible contribution not yet considered is the change of solvation energy. The assembly process involves a change of the solvent environment for the nanoparticles, which could contribute to the change in enthalpy. A more in-depth theoretical modeling of the assembly process is part of our ongoing investigation.

Conclusions

The assessment of the kinetic and thermodynamic factors governing the mediator–template assembly of nanoparticles into spherical assemblies in solutions has led to two important conclusions. First, the mediator–template assembly of nanoparticles is an enthalpy-driven process. Second, the enthalpy change (-1.3 kcal/mol) is close to the magnitude of the van der Waals interaction energy for alkyl chains and the condensation energy of hydrocarbons. Work is in progress to delineate the roles of the mediation and the van der Waals interaction underlying the kinetic process and chemical equilibrium of the mediator–template assembly, along with a systematic correlation of the thermodynamic parameters with the particle size, the chemical nature of the mediator and template agents, and the associated solvation properties.

Acknowledgment. This work was supported by the National Science Foundation (CHE-0349040) and in part by 3M Corporation. The thioether ligand used in this work was synthesized in the laboratory of Dr. D. Rabinovich at the University of North Carolina–Charlotte. M.M.M. thanks the Department of Defense for National Defense Science & Engineering Graduate Fellowship support sponsored by A.R.O.

References and Notes

- (1) (a) Templeton, A. C.; Wuelfing, W. P.; Murray, R. W. *Acc. Chem. Res.* **2000**, *33*, 27. (b) El-Sayed, M. A. *Acc. Chem. Res.* **2004**, *37*, 326. (c) Daniel, M. C.; Astruc, D. *Chem. Rev.* **2004**, *104*, 293.
- (2) (a) Brust, M.; Walker, M.; Bethell, D.; Schiffrin, D. J.; Whyman, R. *J. Chem. Soc., Chem. Commun.* **1994**, 801. (b) Fink, J.; Kiely, C. J.; Bethell, D.; Schiffrin, D. J. *Chem. Mater.* **1998**, *10*, 922. (c) Hostetler, M. J.; Wingate, J. E.; Zhong, C. J.; Harris, J. E.; Vachet, R. W.; Clark, M. R.; Londono, J. D.; Green, S. J.; Stokes, J. J.; Wignall, G. D.; Glush, G. L.; Porter, M. D.; Evans, N. D.; Murray, R. W. *Langmuir* **1998**, *14*, 17. (d) Maye, M. M.; Zheng, W. X.; Leibowitz, F. L.; Ly, N. K.; Zhong, C. J. *Langmuir* **2000**, *16*, 490. (e) Maye, M. M.; Zhong, C. J. *J. Mater. Chem.* **2000**, *10*, 1895. (f) Thomas, K. G.; Zajicek, J.; Kamat, P. V. *Langmuir* **2002**, *18*, 3722. (g) Saunders, A. E.; Sigman, M. B., Jr.; Korgel, B. A. *J. Phys. Chem. B* **2004**, *108*, 193.
- (3) Alivisatos, A. P.; Johnsson, K. P.; Peng, X. G.; Wilson, T. E.; Loweth, C. J.; Bruchez, M. P.; Schultz, P. G. *Nature* **1996**, *382*, 609.
- (4) (a) Hostetler, M. J.; Green, S. J.; Stokes, J. J.; Murray, R. W. *J. Am. Chem. Soc.* **1996**, *118*, 4212. (b) Ingram, R. S.; Hostetler, M. J.; Murray, R. W. *J. Am. Chem. Soc.* **1997**, *119*, 9175. (c) Hostetler, M. J.; Templeton, A. C.; Murray, R. W. *Langmuir* **1999**, *15*, 3782. (d) Templeton, A. C.; Hostetler, M. J.; Kraft, C. T.; Murray, R. W. *J. Am. Chem. Soc.* **1998**, *120*, 1906. (e) Templeton, A. C.; Hostetler, M. J.; Warmoth, E. K.; Chen, S.; Hartshorn, C. M.; Krishnamurthy, V. M.; Forbes, M. D. E.; Murray, R. W. *J. Am. Chem. Soc.* **1998**, *120*, 4845.
- (5) (a) Zamborini, F. P.; Hicks, J. F.; Murray, R. W. *J. Am. Chem. Soc.* **2000**, *122*, 4514. (b) Templeton, A. C.; Zamborini, F. P.; Wuelfing, W. P.; Murray, R. W. *Langmuir* **2000**, *16*, 6682. (c) Musick, M. D.; Pena, D. J.; Botsko, S. L.; McEvoy, T. M.; Richardson, J. N.; Natan, M. J. *Langmuir* **1999**, *15*, 844.
- (6) Leibowitz, F. L.; Zheng, W. X.; Maye, M. M.; Zhong, C. J. *Anal. Chem.* **1999**, *71*, 5076.
- (7) Zheng, W. X.; Maye, M. M.; Leibowitz, F. L.; Zhong, C. J. *Anal. Chem.* **2000**, *72*, 2190.
- (8) Han, L.; Luo, J.; Kariuki, N. N.; Maye, M. M.; Jones, V. W.; Zhong, C. J. *Chem. Mater.* **2003**, *15*, 29.
- (9) Han, L.; Maye, M. M.; Leibowitz, F. L.; Ly, N. K.; Zhong, C. J. *J. Mater. Chem.* **2001**, *11*, 1258.
- (10) Maye, M. M.; Luo, J.; Han, L.; Zhong, C. J. *Nano Lett.* **2001**, *1*, 575.
- (11) Han, L.; Wu, W.; Kirk, F. L.; Luo, J.; Maye, M. M.; Kariuki, N. N.; Lin, Y.; Wang, C.; Zhong, C. J. *Langmuir* **2004**, *20*, 6019.
- (12) (a) Mirkin, C. A.; Letsinger, R. L.; Mucic, R. C.; Storhoff, J. J. *Nature* **1996**, *382*, 607. (b) Elghanian, R.; Storhoff, J. J.; Mucic, R. C.; Letsinger, R. L.; Mirkin, C. A. *Science* **1997**, *277*, 1078. (c) Taton, T. A.; Mucic, R. C.; Mirkin, C. A.; Letsinger, R. L. *J. Am. Chem. Soc.* **2000**, *122*, 6305–6306.
- (13) Wang, G.; Murray, R. W. *Nano Lett.* **2004**, *4*, 95.
- (14) (a) Boal, A. K.; Ilhan, F.; DeRouchey, J. E.; Thurn-Albrecht, T.; Russell, T. P.; Rotello, V. M. *Nature* **2000**, *404*, 746. (b) Boal, A. K.; Rotello, V. M. *J. Am. Chem. Soc.* **2002**, *124*, 5019.
- (15) (a) Frankamp, B. L.; Boal, A. K.; Rotello, V. M. *J. Am. Chem. Soc.* **2002**, *124*, 15146. (b) Kariuki, N. N.; Han, L.; Ly, N. K.; Peterson, M. J.; Maye, M. M.; Liu, G.; Zhong, C. J. *Langmuir* **2002**, *18*, 8255.
- (16) Maye, M. M.; Chun, S. C.; Han, L.; Rabinovich, D.; Zhong, C. J. *J. Am. Chem. Soc.* **2002**, *124*, 4958.
- (17) Maye, M. M.; Luo, J.; Lim, I.-I. S.; Han, L.; Kariuki, N. N.; Rabinovich, D.; Liu, T.; Zhong, C. J. *J. Am. Chem. Soc.* **2003**, *125*, 9906.
- (18) Han, L.; Daniel, D. R.; Maye, M. M.; Zhong, C. J. *Anal. Chem.* **2001**, *73*, 4441.
- (19) (a) Zamborini, F. P.; Leopold, M. C.; Hicks, J. F.; Kulesza, P. J.; Malik, M. A.; Murray, R. W. *J. Am. Chem. Soc.* **2002**, *124*, 8958. (b) Leopold, M. C.; Donkers, R. L.; Georganopoulou, D.; Fisher, M.; Zamborini, F. P.; Murray, R. W. *Faraday Discuss.* **2004**, *125*, 63.
- (20) (a) Israel, L. B.; Kariuki, N. N.; Han, L.; Maye, M. M.; Luo, J.; Zhong, C. J. *J. Electroanal. Chem.* **2001**, *517*, 69. (b) Kariuki, N. N.; Luo, J.; Han, L.; Maye, M. M.; Moussa, L.; Patterson, M.; Lin, Y.; Engelhard, M. H.; Zhong, C. J. *Electroanalysis* **2004**, *16*, 120.
- (21) Zhong, C. J.; Luo, J.; Maye, M. M.; Han, L.; Kariuki, N. N. Nanostructured Gold and Alloy Electrocatalysts. In *Nanotechnology in Catalysis*; Zhou, B.; Hermans, S.; Somorjai, G. A., Eds.; Kluwer Academic/Plenum Publishers: New York, 2004; Vol. 1, Chapter 11, pp 222–248.
- (22) Narayanan, R.; El-Sayed, M. A. *J. Am. Chem. Soc.* **2004**, *126*, 7194.
- (23) (a) Maye, M. M.; Lou, Y.; Zhong, C. J. *Langmuir* **2000**, *16*, 7520. (b) Zhong, C. J.; Maye, M. M. *Adv. Mater.* **2001**, *13*, 1507.
- (24) (a) Maye, M. M.; Luo, J.; Lin, Y.; Engelhard, M. H.; Hepel, M.; Zhong, C. J. *Langmuir* **2003**, *19*, 125. (b) Luo, J.; Maye, M. M.; Lou, Y.; Han, L.; Hepel, M.; Zhong, C. J. *Catal. Today* **2002**, *77*, 127. (c) Maye, M. M.; Luo, J.; Han, L.; Kariuki, N. N.; Zhong, C. J. *Gold Bull. (London)* **2003**, *36*, 75.
- (25) (a) Chen, S. *Langmuir* **2001**, *17*, 6664. (b) Chen, S. *J. Am. Chem. Soc.* **2000**, *122*, 7420. (c) Chen, S.; Yang, Y. *J. Am. Chem. Soc.* **2002**, *124*, 5280. (d) Hicks, J. F.; Zamborini, F. P.; Osisek, A. J.; Murray, R. W. *J. Am. Chem. Soc.* **2001**, *123*, 7048.
- (26) Zheng, W. X.; Maye, M. M.; Leibowitz, F. L.; Zhong, C. J. *Analyst (Cambridge, U. K.)* **2000**, *125*, 17.
- (27) Landes, C.; El-Sayed, M. A. *J. Phys. Chem. A* **2002**, *106*, 7621.
- (28) Yim, H. W.; Tran, L. M.; Dobbin, E. D.; Rabinovich, D.; Liable-Sands, L. M.; Incavito, C. D.; Lam, K.-C.; Rheingold, A. L. *Inorg. Chem.* **1999**, *38*, 2211.
- (29) Maye, M. M.; Han, L.; Kariuki, N. N.; Ly, N. K.; Chan, W.-B.; Luo, J.; Jones, V. W.; Zhong, C. J. *Anal. Chim. Acta* **2003**, *496*, 17.
- (30) (a) Link, S.; El-Sayed, M. A. *Int. Rev. Phys. Chem.* **2000**, *19*, 409. (b) Papavassiliou, G. C. *Prog. Solid State Chem.* **1979**, *12*, 185.
- (31) Luo, J.; Maye, M. M.; Han, L.; Kariuki, N. N.; Jones, V. W.; Lin, Y. H.; Engelhard, M. H.; Zhong, C. J. *Langmuir* **2004**, *20*, 4254.
- (32) (a) Storhoff, J. J.; Lazarides, A. A.; Mucic, R. C.; Mirkin, C. A.; Letsinger, R. L.; Schatz, G. C. *J. Am. Chem. Soc.* **2000**, *122*, 4640. (b) Haes, A. J.; Van Duyne, R. P. *J. Am. Chem. Soc.* **2002**, *124*, 10596. (c) Ung, T.; Liz-Marzan, L.; Mulvaney, P. *J. Phys. Chem. B* **2001**, *105*, 3441.
- (33) Weisbecker, C. S.; Merritt, M. V.; Whitesides, G. M. *Langmuir* **1996**, *12*, 3763.
- (34) (a) Nuzzo, R. G.; Dubois, L. H.; Allara, D. L. *J. Am. Chem. Soc.* **1990**, *112*, 558. (b) Cogen, J. M.; Maier, W. F. *Langmuir* **1987**, *3*, 830.